This is the Pre-Published Version.
The following publication Y. Yang, K. -I. Yung, R. T. W. Hung, J. A. Foster and K. -M. Yu, "Surface Model Extraction from Indentation Curves of Hyperelastic Simulation for Abnormality Detection," 2019 International Symposium on Medical Robotics (ISMR), Atlanta, GA, USA, 2019, pp. 1-7 is available at https://doi.org/10.1109/ISMR.2019.8710188.

Surface Model Extraction from Indentation Curves of Hyperelastic Simulation for Abnormality Detection

Yingqiao Yang, Kai-leung Yung, Robert Tin Wai Hung, James Abbott Foster, Kai-Ming Yu
Department of Industrial and Systems Engineering
The Hong Kong Polytechnic University, Hong Kong
robert.tw.hung@polyu.edu.hk

***Abstract*—Manual palpation for the detection of anomalies is not possible through the small incisions of Robotic Minimally Invasive Surgery. The proposed novel approach allows robotic palpation by deforming the tissue surface with an indenter and analyzing the corresponding induced surface shape for indications of the abnormalities underneath. Three-dimensional hyperelastic finite element models were used to simulate the tool-tissue interaction of a hemispherical indenter pushing downwards onto the tissue surface. Curve fitting methods were employed to characterize the indentation curve of the deformed surface of either normal or abnormal tissue with an empirical equation. By analyzing these equations, we developed volume-based and gradient-based methods to investigate how the tumor position affects the surface deformation behavior of the tissue.**

The results of the simulations indicate that there are obvious differences in the surface deformation between healthy and diseased tissue, due to the higher stiffness of the tumor. A significant advantage of the proposed method is that it greatly broadens the detection area by providing estimates on the direction and distance of the tumor from the surrounding area of the indentation site, compared with previous studies only predicting the presence of a tumor in the contact area.

***Index Terms*—Robotic Minimally Invasive Surgery (RMIS), Finite-Element (FE) modeling, tumor detection, deformable surface modeling**

I. Introduction

Sophisticated imaging techniques such as magnetic resonance imaging (MRI) or computed tomography (CT) scanning have made it possible to preoperatively detect the existence of a tumor and show its approximate location inside of human body. However, during the surgical procedure, the location of a tumor is often different from that in a preoperative scan due to the deformability of soft tissue and organ movement. As a result, operations such as tumor resection require the surgeons to locate the exact tumor position intraoperatively [1], [2].

Since tumors are typically stiffer than their surrounding tissue [3], [4], in traditional open surgery a large incision is introduced so that surgeons' hands can access the surgical site to confirm the location of the tumor by direct palpation. However, the large incision often leads to a high risk of infection and long recovery time. The emergence of Minimally Invasive Surgery (MIS) has allowed surgeries to be performed through a small incision but the surgeons' hands are separated from the surgical site, meaning surgeons can only palpate tissue through long slim medical instruments [5], [6]. Moreover, surgeons in MIS often suffer from poor ergonomic positions and unstable visual feedback from a hand-held endoscopic camera. The recent advancements of Robotic-assisted Minimally Invasive Surgery (RMIS) have improved surgical performance but the master-slave mode of the operation in RMIS procedures further restricts a surgeon's sensation of palpation [7], [8]. Visual cues lead surgeons to tumors on the surface of organs but deeper tumors will not be easily located.

Against the above background, a new method is required to facilitate surgeons in RMIS to intraoperatively detect the tumor buried in normal tissue. Most existing approaches are based on direct stiffness measurement where an indenter is employed to deform the soft tissue and the stiffness at the contact point is measured by dividing the applied force by the displacement of the indenter tip. Ahn et al. [9] proposed an approach that employing robotic scanning and sweeping to detect the presence of hard inclusions embedded in a silicone phantom by measuring the force responses at different indentation depth. Yamamoto et al. [10] employed a vertical robotic palpation device to automatically estimate tissue properties and detect a hard object hidden in artificial tissue. Since these discrete uniaxial indentation methods may be time-consuming and not efficient in investigating large tissue area to examine a tumor, Liu and colleagues [11] proposed an approach that moved a force-sensed roller over a tissue surface to rapidly obtain a continuous stiffness distribution. However, in their study, a constant indentation depth was required during the rolling procedure, which is not practical in real applications [12]. The issue of whether to use a constant force or constant displacement is quite clear in a clinical surgical operation where a live organ moves constantly and hence it is very difficult or impractical to maintain a constant distance or indentation depth from the organ/tissue while applying a constant force is much easier. More recent research on tumor detection employing robotic palpation can be found in [13]–[15]. Based on the observation of the coupling effect, where soft tissue deforms not only at the point of force application but also at its surrounding area, Tanaka et al. [16] suggested that it was not accurate to obtain a tissue's stiffness directly

The work described in this paper was mainly supported by a grant from the Research Committee of The Hong Kong Polytechnic University under student account code RUMP.

©2019 IEEE. Personal use of this material is permitted. Permission from IEEE must be obtained for all other uses, in any current or future media, including reprinting/republishing this material for advertising or promotional purposes, creating new collective works, for resale or redistribution to servers or lists, or reuse of any copyrighted component of this work in other works.

using force divided by the displacement at the contact point. Kawahara et al. [17] used a non-contact stiffness imager to detect the abnormality, where an air jet force was exerted on the soft tissue and the stiffer point underneath could be detected by analyzing the displacement distribution of the resultant deformed surface. However, they did not give a quantitative estimation of the tumor's location.

From previous researches, we can see that the neighborhood area around the force application point contains important information for tumor detection. Considering the direct contact approach has higher accuracy and resolution with a relatively stable deformed surface, we have chosen the approach of exerting a constant force indenter on the soft tissue and extracting the resultant deformed surface for modeling and analysis. Since the tumor is typically stiffer than its surrounding tissue, significant visual differences between the Deformed Surface of the Normal tissue (DSN) and the Deformed Surface of the Abnormal tissue (DSA) can be captured by utilizing the existing high-quality visual tools in RMIS.

In this study, to assess the theory of tumor detection through indentation, we first use a computer simulation for surface model extraction and analysis in an ideal environment with clean surface data. It is appropriate in the development of the surface representation and tumor detection method to reduce possible noise and bias to the data at this stage. First of all, 3D hyperelastic finite element (FE) simulation models of normal and abnormal tissue were constructed to establish an initial understanding of the tool-tissue interaction. The DSN and DSA were generated from the simulator by applying a hemispherical indenter into the soft tissue at a constant force. Then the indentation curve data, sets of curves running from the center of the indenter and extending radially, were extracted from the DSN and DSA as the features of the deformed surfaces. After characterizing these curves via the fitting of functions to the curve data, the whole deformed surface was modeled. Finally, by analyzing the physical differences between the DSN and DSA, volume-based and gradient-based methods were investigated to estimate the tumor's location quantitatively.

II. Methods

A. FE Modeling of Tool-tissue Interaction

In this paper, the Arruda-Boyce model is selected to characterize the mechanical behavior of the soft tissue, since this model is reported to be suitable to estimate relatively large tissue deformation [**?**], [18]. The Arruda-Boyce model is also called the eight-chain model, representing the molecular network of rubber employing an eight-chain configuration, only requiring two parameters (shear modulus and locking stretch) to describe the nonlinear and hyperelastic material behavior [19]. Many previous researchers have studied soft tissue based on this model [20]–[22]. Sangpradit et al. [22] conducted uniaxial compression experiments and employed an inverse FE method to obtain the material properties of normal and abnormal tissue based on the Arruda-Boyce model. From their paper, the shear modulus and locking stretch for the normal tissue were set as 4.98 kPa and 1.05 respectively; for the tumor, they were 73.4 kPa and 1.01 respectively.

3D FE tool-tissue interaction models were constructed in order to establish an understanding of the soft tissue's response to indentation. Since healthy abdominal tissue such as liver and kidney is usually assumed to be approximately isotropic, homogeneous, and incompressible, in this study [23], a homogeneous deformable cube with dimension 30 mm (height) × 100 mm (length) × 80 mm (width) was designed to simulate the normal tissue with an FE mesh of eight-node linear brick 3D stress hexahedron (Abaqus element type C3D8R), shown in Fig. 1a. Fig. 1b and c show the model from the top view and side view. The region close to the indenter was more meshed with a finer element size of 0.6mm to acquire more accurate results. The indenter was modeled as a 3D analytical rigid shell with a hemispherical bottom 6 mm in diameter.

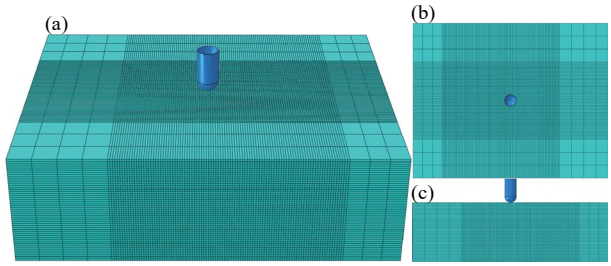

Fig. 1. (a) a 3D FF model for tool-normal tissue interaction, (c) the model from the top view, (c) from the side view.

In most clinical scenarios, tumors located at liver or kidney are trend to be spherical and larger than 10 mm in size. Therefore, for tumorous tissue modeling, we designed the tumor as a sphere ball with 10 mm in diameter (see Fig. 2a) to estimate our localization methods under a worse circumstance [24], [25]. Fig. 2b and c show the location of the tumor from the top view and side view, where the tumor's distance, from the center of the tumor to center of the indenter, is 6 mm; and the tumor's depth, from the center of the tumor to the tissue surface is 8 mm. The contact between the tissue and the indenter was defined as surface-to-surface contact without friction. The bottom of the tissue was set as fixed, and the concentrate load applied on the indenter tip was in the normal direction to the surface. During the tool-tissue interaction, the amplitude of the load increased from 0 to 4N linearly.

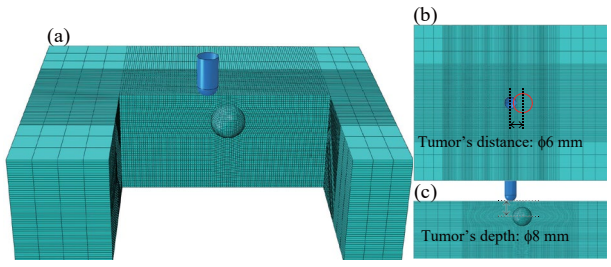

Fig. 2. (a) a 3D FF model for tool-abnormal tissue interaction, (c) the model from the top view (c) from the side view.

B. Indentation Curve Extraction and Characterization

After indented the normal tissue with a force load of 4 N, a deformed surface is formed around the indenter. Fig. 3a and c show the deformed surface from the side view and top view. The deformed surface was further extract in the form of 3D point cloud data ignoring nodes occluded by the bottom of the indenter and those with little deformation. As a result, all valid nodes located outside the white circle (3 mm in radius) and inside the yellow circle (20 mm in radius) were acquired to represent the deformed surface, which is shown as Fig. 3b, including around 3700 nodes.

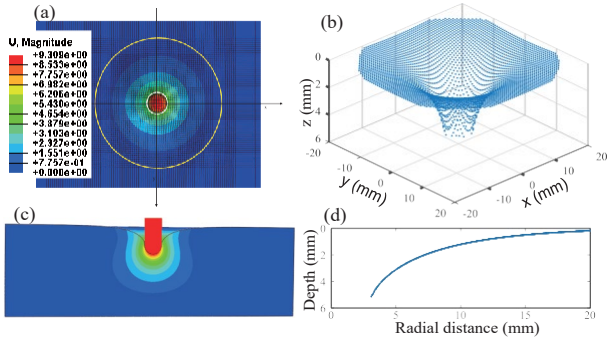

Fig. 3. (a) A DSN from the top view, (c) point cloud data of the DSN, (b) a DSN from the side view, (d) the indentation curve of DSN.

To further investigate the deformed surface, we naturally select indentation curves, running from the center of the indenter and extending radially, as the features of the surface. The point cloud data in Cartesian coordinates (x, y, z) were transformed into cylindrical coordinates (r, , z) to extract the indentation curves. After plotting the surface deflection depth z with respect to their radial distances r in all , all valid nodes converge onto one curve as shown in Fig. 3d, which indicates the symmetry of the DSN due to homogenous and isotropic properties of the normal tissue. Given that the DSN can be represented by revolving this indentation curve, it can thus act as a feature of DSN.

With a tumor embedded in, the soft tissue becomes heterogeneous. After the coordinate transformation, the valid nodes on the DSA are plotted as shown in Fig. 4a. The dispersion of those valid nodes indicates the asymmetry of the DSA. Since the DSA is asymmetric, it cannot be represented by only one indentation curve. To find out the surface features on the DSA, we divided the whole surface into twelve partitions, shown in Fig. 4b, where the green circle indicates the location of the indenter from the top view, and the red circle gives the location of the tumor. We collect the valid nodes on each partition and then plotted the graph of deflection depth against the radial distance for each individual partition, as in Fig. 4c. Since each converged indentation curve can act as the feature of its own partition, the DSA can thus be represented by combining these twelve indentation curves.

With these indentation curves, the complex deformed behavior of soft tissue can be abstractly represented. By characterizing these curves using mathematical equations, one can

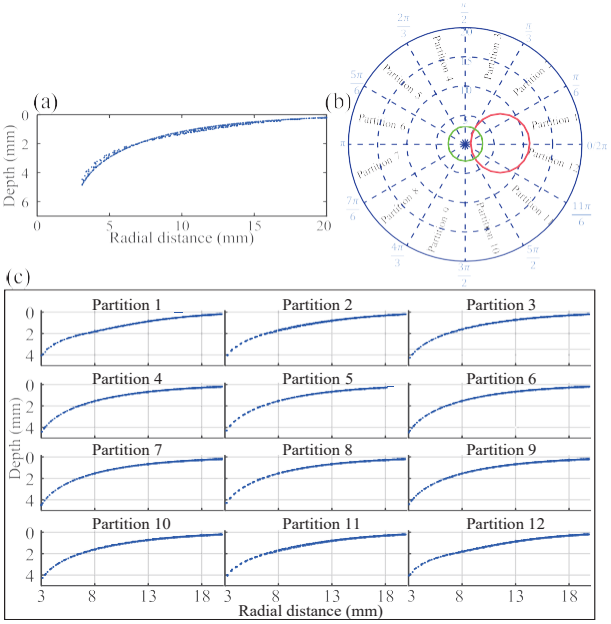

Fig. 4. (a) valid nodes on DSA after coordinates transformation, (b) surface partition, (c) valid nodes on each partition.

determine their important characteristics, which can be further used for mathematically modeling the whole deformed surface. Seven empirical mathematical models were selected in our investigation, listed in Table I. $\hat{d}$ is the estimated surface deflection depth with respect to a given radial distance r. $\hat{a}$, $\hat{c}$, $\hat{k}$, $\hat{n}$ and are the unknown parameters to be estimated.

In order to determine which model is the most appropriate to characterize the indentation curves, we evaluated these six models for their ability to fit the dataset accurately and consistently. It is noted that the indentation curves on DSN and DSA are expected to be characterized by the same model to keep the consistency for later analysis. Therefore, in this study, the datasets for model evaluation were obtained from DSN tested under different force loads. Once the best model is confirmed, it is also applied to fit the indentation curves on DSA to check the quality of the fitting. The fitting was measured by one indicator: Root Mean Squared Error (RMSE).

C. Deformed Surface Modeling and Abnormality Detection

With known indentation curve equations, we employed double integrals in cylindrical coordinates to model DSN and DSA by calculating the deformed volume of them. Let $f_{normal}(r, \theta)$ denote the characterized equation of the indentation curve of DSN, where r is the radial distance varying from 3 mm to 20 mm and θ is the direction of the indentation curve, ranging from 0 to 2π. V_{normal}, the deformed volume of DSN, is given by:

$$V_{normal} = \int_{\theta_0}^{\theta_1} \int_{r_0}^{r_1} f_{normal}(r, \theta) r dr d\theta \qquad (1)$$

For the DSA, since it was divided into twelve partitions, the modeling equation should integrate all indentation curves. Let

$f_j(r, \theta)$ be the characterized equation of indentation curve of surface partition j, $j = 1 \quad 12$. v_j, the volume of the surface partition j is given as (3), where r is from 3 mm to 20 mm and θ is from 0 to $\pi/6$. Let $v_{abnormal}$ denote the deformed volume of the DSA. It is given by

$$v_j = \int_{\theta_0}^{\theta_1} \int_{r_0}^{r_1} f_j(r, \theta) r dr d\theta \qquad (2)$$

$$V_{abnormal} = \sum_{j=1}^{12} v_j \qquad (3)$$

Based on the above mathematical descriptions of the DSN and DSA, the deformed volume of tissue within a defined range of space can be determined. Thus, it allows us to evaluate the physical difference between the DSN and DSA by calculating their volumetric difference, which paves the way for further quantitative tumor estimation since it is the tumor's existence that leads to that difference. Subsequently, we investigated the volume of each partition of the DSA, as well as the volume difference between DSN and DSA to see whether these measures were able to relate to the tumor's location. The detailed results can be found SectionIII-B.

Motivated by the observations that the rate of change along the curves varies between different partitions of the DSA, we further investigated another abstract approach based on the gradient of the indentation curves. As shown in Fig. 5, the characterized indentation curves of partition 1, 2 and 7 of the DSA are presented. It can be seen that the tumor's existence reduces the gradient at the starting point of the indentation curves since partition 1 and 2 are tumorous, compared with partition 7, the normal partition represented by a steeper curve. Given that the tumor's existence often leads to the increase in stiffness of soft tissue, the gradient of the indentation curves may have some physical reference to the stiffness. Let's define the gradient at the starting point of the indentation curve as overall stiffness indicator (OSI), $OSI = \partial f_j / \partial r$ (at $r = 3mm$), which can serve as useful scalars for roughly approximating overall stiffness of each partition. Based on the changes in stiffness, one can estimate the possible location of the tumor.

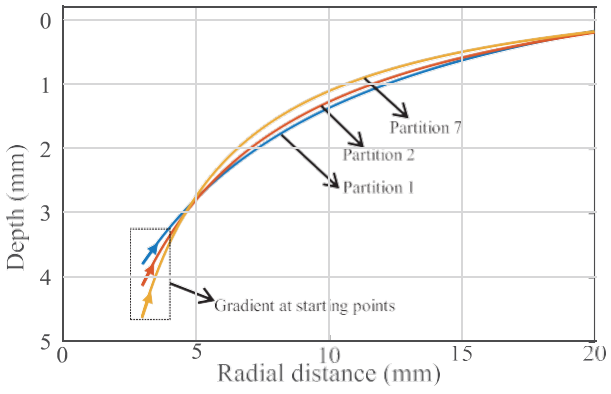

Fig. 5. The indentation curves of DSA at partition 1, 2 and 7.

III. Result

A. Indentation Curve Characterization

Six indentation tests were performed on the normal tissue and the applied force load increased linearly from 1N to 6N with 1N increment. The indentation curves were extracted from DSN under varied force loads as datasets for mathematical model estimation. The six proposed models in Table I were evaluated according to their abilities to fit these indentation curves, and RMSE of six tests were averaged for each model. A hyperbola model was selected as the best one to characterize the indentation curve.

TABLE I
Six Empirical Models and Comparison of RMSE

Model name	Equation of model	RMSE
2nd polynomial	$d = \hat{a}_0 + \hat{a}_1 r + \hat{a}_2 r^2$	0.138
3rd polynomial	$d = \hat{a}_0 + \hat{a}_1 r + \hat{a}_2 r^2 + \hat{a}_3 r^3$	0.058
4th polynomial	$d = \hat{a}_0 + \hat{a}_1 r + \hat{a}_2 r^2 + \hat{a}_3 r^3 + \hat{a}_4 r^4$	0.028
2nd power	$d = \hat{c} + k r^n$	0.021
Hyperbola	$d = \hat{c} + k/(r + b)$	0.017
Exponential	$d = \hat{c} + k e^{br}$	0.051

To further verify the applicability of the hyperbola model, we also employed the indentation curves on DSN resulted from different force loads (1N, 2N, ..., 4N) using the indenter with various diameters (5mm, 6mm, ..., 10mm) as datasets for testing. The results indicate that the hyperbola model has a good performance to characterize the indentation curves in different circumstances.

For the abnormal tissue shown in Fig. 2a, the deformed surface resulted from a 6 mm indenter with a force load of 4N is partitioned into twelve portions. The hyperbola model was used to characterize corresponding twelve indentation curves. The fitting results are shown in Table II, implying the hyperbola model's good fitting ability for indentation curves of DSA.

TABLE II
The Unknown Parameters Estimation Results of Indentation Curves on the DSA

Partition #	$\hat{c}$	$\hat{k}$	$\hat{b}$	RMSE
1	-1.739	49.708	6.086	0.048
2	-1.223	32.866	3.256	0.036
3	-0.926	24.196	1.63	0.02
4	-0.844	21.762	1.15	0.013
5	-0.835	21.306	1.043	0.012
6	-0.836	21.245	1.022	0.012
7	-0.829	21.079	0.982	0.013
8	-0.835	21.306	1.043	0.012
9	-0.844	21.76	1.149	0.013
10	-0.926	24.197	1.63	0.02
11	-1.223	32.871	3.257	0.036
12	-1.747	49.872	6.075	0.047

B. Abnormality Detection

For in-situ tumor localization, the main objective is to guide the surgeon to approach the tumor. Given that the size and

depth of the tumor are known preoperatively, it is critical to estimate tumor's distance, the radial distance from the center of the indenter to the center of the tumor, and tumor's direction, the possible located partitions. To investigate the method proposed in Section II-C, we constructed abnormal tool-tissue interaction model with varied tumor's distance from 0 mm to 20 mm. At each location, the indentation curves on DSA under a constant force load of 4N were acquired and characterized. Fig. 6 shows the valid nodes of each case, including normal tissue and abnormal tissue. In Fig. 6a where tumor's distance is 0 mm, all valid nodes also converge like that on the normal tissue, which indicates that deformed surface is also symmetric due to the even distribution of the tumor in each partition. However, the gradient of the converged curve has an obvious deviation compared with that of normal tissue. Moreover, from Fig. 6c to g, the dispersion of the valid nodes reduces with the increase in tumor's distance, and from Fig. 6h to l, it can be seen that when the tumor's distance is larger than 10 mm, there is no obvious dispersion, which may indicate the possible detectable region of the tumor.

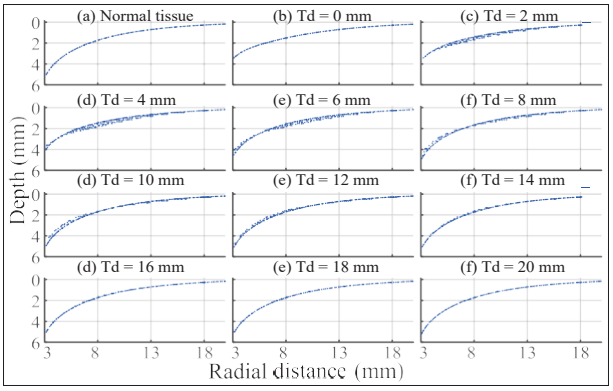

Fig. 6. All valid nodes on the DSN and DSA with the tumor's distance varying from 0 mm to 20 mm (Td is the tumor's distance).

1) Volume-based analysis: Since it is the tumor that leads to the difference between DSN and DSA, one straightforward tumor detection method is to quantify the difference and then relate it to the tumor's location. The deformed volume of DSN and DSA have been modeled according to (1)-(3), making it possible to analyze the difference based on volume quantitatively, and further investigate tumor's location.

The partition volume of DSA for all cases was shown in Fig. 7a. It can be seen that when the tumor's distance is 0 mm, due to the even distribution of the tumor, the volume of each partition is almost identical, but much smaller compared with the volume of normal tissue. When the tumor's distance varies from 2 mm to 10 mm, the existence of the tumor results in the increase in partition volume. Taking the yellow curve as an example, the volume of tumorous partitions 1 and 12 is much larger than the healthy partitions 6 and 7. Additionally, the volume reduces smoothly from the abnormal partition to the normal one, which is corresponding to the decrease in the proportion of the tumor, also indicating the consistency of the soft tissue. By finding out the partitions with the least volume, one can thus define the healthy partitions that are shown in the dash-dotted rectangle box in Fig. 7a. It should be mentioned that when the tumor's distance is larger than 10 mm, there is no obvious change in partition volume, which coincides with the observation in Fig. 6.

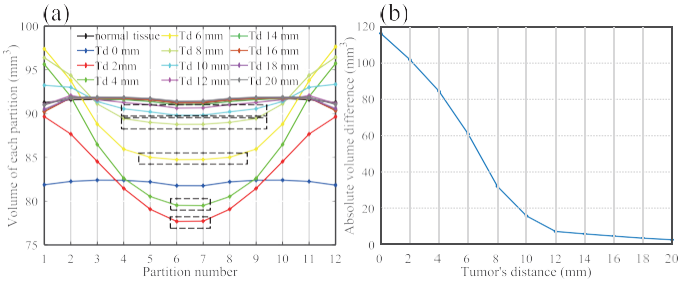

Fig. 7. (a) The volume of each partition of DSN and all DSA, (b) The total absolute volume differences between DSN and all DSA.

Subsequently, the volume differences between DSN and DSA were investigated to estimate the tumor's horizontal distance from the center of the indenter. The absolute difference was given by (4)-(5), where $(v_{ij})_{absdiff}$ denotes the absolute volume difference between the normal and abnormal tissue in the partition j ($j = 1, 2...12$); i is the tumor's distance ($i = 0, 2...20$); $(V_i)_{absdiff}$ denotes the overall absolute volume difference between normal and abnormal tissue.

$$(v_{ij})_{absdiff} = \left|(v_{ij})_{abnormal} - (v_j)_{normal}\right| \quad (4)$$

$$(V_i)_{absdiff} = \sum_{j=1}^{12} (v_{ij})_{absdiff} \quad (5)$$

The results of volume differences with respect to tumor's distance are shown in Fig. 7b. It can be seen that when the tumor's distance is within 10 mm, the absolute volume difference decreases approximately linearly with the increase in tumor's distance, and can thereby serve as an indicator to estimate the tumor's distance from the center of the indenter. When the tumor's distance is larger than 10 mm, there are no obvious differences in volume between normal tissue and abnormal tissue. From the quasi-linear part of the curve in Fig. 7b, an empirical equation can be generated to relate the absolute volume difference to the tumor's distance, for this set of data (see Table III)

2) Gradient-based analysis: This section details a less-computationally intensive approach to estimate the tumor's location, which is achieved by applying the OSI measurement to the indentation curves. As the overall stiffness of each partition could be approximately represented by an OSI value, the abnormal partitions could be found by investigating these values. Moreover, with further analysis, the tumor's distance can also be estimated.

The OSI value of each partition is plotted with respect to the partition number as in Fig. 8a. The result shows that partitions with a lower value in OSI have a higher possibility to be abnormal, whilst normal partitions, or partitions that only contain a small part of the tumor, exhibit a higher value in

OSI. In term of physical interpretation, a lower OSI indicates a higher stiffness of its corresponding portion of the soft tissue. Through lateral comparison of each curve in Fig. 8a, the healthy partitions with maximum OSI can thus be estimated as shown in the dash-dotted.

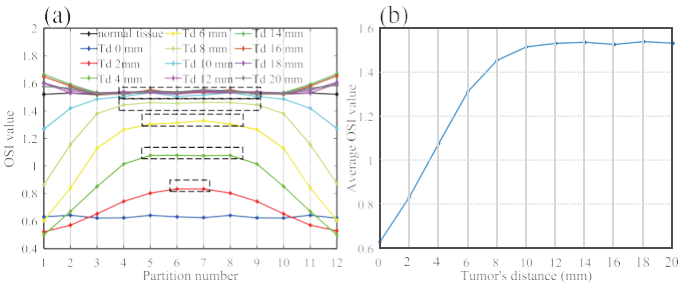

Fig. 8. (a) OSI value of each partition of DSN and all DSA, (b) The average OSI value of defined healthy partitions on all DSA.

Through the vertical comparison of the defined healthy partitions of each curve, one can see that their average OSI value rises gradually with the increase in tumor's distance. Fig. 8b shows the average OSI value with respect to the tumor's distance. It is shown that when the tumor's distance is within 10 mm, the OSI rises observably with the increase in tumor's distance, which may indicate that the tissue becomes softer with the tumor moving away from the indenter center. Therefore, through the vertical comparison of each curve, the tumor's distance can be estimated. It is also noted that there are no obvious changes in the average OSI when the tumor's distance is larger than 10 mm, which agrees with the observation in the volume-based analysis. Considering the curve in Fig. 8b is nonlinear when tumor's distance varies from 0 mm to 10 mm, a second order polynomial equation is employed to relate the average OSI value to the tumor's distance (see Table III).

TABLE III
EMPIRICAL EQUATIONS FOR TUMOR'S DISTANCE ESTIMATION

Approach	Empirical equation
Volume-based analysis	$Td = -0.0946V + 11.47$
Gradient-based analysis	$Td = 5.367I^2 - 1.234I - 1.095$

V is the deformed volume of DSA
I is the average OSI of the healthy partitions on DSA

IV. DISCUSSION AND CONCLUSION

This paper reports a novel approach for tumor localization in RMIS by investigating the DSN and DSA formed during the tool-tissue interaction. All analysis were based on the 3D hyperelastic FE simulated data. The indentation curves on DSN and DSA were extracted as features of the deformed surfaces and then characterized by a hyperbolic equation. Based on these characterized indentation curves, volume-based analysis and gradient-based analysis were developed to estimate the position of the tumor. The results indicate that differences in the surface deformation between healthy and diseased tissue can be quantified with respect to the tumor's location on the DSA tissue.

As for the two developed tumor localization methods, both of them are capable of estimating tumor's direction and horizontal distance from the indenter center. However, the data collected from the real scenario are often polluted by noise, causing the characterized indentation curve to deviate from the real one. By integration, the volume-based method accumulates the deviation in practical applications, leading to an error-prone estimation. Moreover, the computational cost is another shortcoming. By contrast, the gradient-based method, with a less computation loading, differentiated based approach, can effectively estimate the tumor's location despite the use of an initial gradient to approximately represent the overall stiffness. This method may be more practical for real applications, which will be validated in further work. It should be mentioned that the detectable region of the abnormality in this study is 10 mm in radius since when the tumor's distance is larger than 10 mm, neither of these two methods works well. The size of the detectable region may also be related to the tumor's size, depth, and stiffness, and is worth further investigation. It is noted that how the variation in the tumor's depth, stiffness and size influence the deformed surface of the soft tissue is not included in our current work. Moreover, in this paper, soft tissue with a flat surface was assumed for simplicity of analysis but the method can be easily extended to curved surfaces. In future work, the geometry of the soft tissue will be involved for more accurate analysis. In addition to that, more real indentation experiments on live soft tissue should be conducted to validate this result.

The emphasis of paper is on the methodology development for tumor detection based on surface deformation modeling. The simulation environment was constructed to provide initial datasets for analysis. Even though the behavior of the soft tissue in a real situation will be slightly different from that in the simulation environment, a similar methodology can be applied to characterize the deformed surface for the abnormality estimation. The significance of this study can be in two aspects: Firstly, it presents the possibility of quantitative in-situ tumor location estimation by modeling and analyzing the deformed surface that enables prediction of the tumor's location in the contact region and the surrounding areas of the indenter. Secondly, the successful development of two tumor localization approaches not only provides information about tissue underneath structures but also contributes to in-situ surgery navigation in optimizing the tumor searching path and defining the boundary of tumor resection.

REFERENCES

[1] S. Jaume, M. Ferrant, B. Macq, L. Hoyte, J. R. Fielding, A. Schreyer, R. Kikinis, and S. K. Warfield, "Tumor detection in the bladder wall with a measurement of abnormal thickness in ct scans," *IEEE Transactions on Biomedical Engineering*, vol. 50, no. 3, pp. 383–390, 2003.

[2] S. Bayer, A. Maier, M. Ostermeier, and R. Fahrig, "Intraoperative imaging modalities and compensation for brain shift in tumor resection surgery," *International journal of biomedical imaging*, vol. 2017, 2017.

[3] S. Phipps, T. Yang, F. Habib, R. Reuben, and S. McNeill, "Measurement of tissue mechanical characteristics to distinguish between benign and malignant prostatic disease," *Urology*, vol. 66, no. 2, pp. 447–450, 2005.

[4] K. Hoyt, B. Castaneda, M. Zhang, P. Nigwekar, P. A. di Sant'Agnese, J. V. Joseph, J. Strang, D. J. Rubens, and K. J. Parker, "Tissue elasticity properties as biomarkers for prostate cancer," *Cancer Biomarkers*, vol. 4, no. 4-5, pp. 213–225, 2008.

[5] S. A. Antoniou, G. A. Antoniou, A. I. Antoniou, and F.-A. Granderath, "Past, present, and future of minimally invasive abdominal surgery," *JSLS: Journal of the Society of Laparoendoscopic Surgeons*, vol. 19, no. 3, 2015.

[6] S. R. Driessen, E. M. Sandberg, S. P. Rodrigues, E. W. Van Zwet, and F. W. Jansen, "Identification of risk factors in minimally invasive surgery: a prospective multicenter study," *Surgical endoscopy*, vol. 31, no. 6, pp. 2467–2473, 2017.

[7] F. P. Prete, A. Pezzolla, F. Prete, M. Testini, R. Marzaioli, A. Patriti, R. M. Jimenez-Rodriguez, A. Gurrado, and G. F. Strippoli, "Robotic versus laparoscopic minimally invasive surgery for rectal cancer: a systematic review and meta-analysis of randomized controlled trials," *Annals of surgery*, vol. 267, no. 6, pp. 1034–1046, 2018.

[8] M. Diana and J. Marescaux, "Robotic surgery," *British Journal of Surgery*, vol. 102, no. 2, pp. e15–e28, 2015.

[9] B. Ahn, Y. Kim, C. K. Oh, and J. Kim, "Robotic palpation and mechanical property characterization for abnormal tissue localization," *Medical & biological engineering & computing*, vol. 50, no. 9, pp. 961–971, 2012.

[10] T. Yamamoto, N. Abolhassani, S. Jung, A. M. Okamura, and T. N. Judkins, "Augmented reality and haptic interfaces for robot-assisted surgery," *The International Journal of Medical Robotics and Computer Assisted Surgery*, vol. 8, no. 1, pp. 45–56, 2012.

[11] H. Liu, D. P. Noonan, B. J. Challacombe, P. Dasgupta, L. D. Seneviratne, and K. Althoefer, "Rolling mechanical imaging for tissue abnormality localization during minimally invasive surgery," *IEEE Transactions on Biomedical Engineering*, vol. 57, no. 2, pp. 404–414, 2010.

[12] M. Li, H. Liu, A. Jiang, L. D. Seneviratne, P. Dasgupta, K. Althoefer, and H. Wurdemann, "Intra-operative tumour localisation in robot-assisted minimally invasive surgery: A review," *Proceedings of the Institution of Mechanical Engineers, Part H: Journal of Engineering in Medicine*, vol. 228, no. 5, pp. 509–522, 2014.

[13] A. Garg, S. Sen, R. Kapadia, Y. Jen, S. McKinley, L. Miller, and K. Goldberg, "Tumor localization using automated palpation with gaussian process adaptive sampling," in *Automation Science and Engineering (CASE), 2016 IEEE International Conference on*. IEEE, 2016, pp. 194–200.

[14] J. Konstantinova, G. Cotugno, P. Dasgupta, K. Althoefer, and T. Nanayakkara, "Palpation force modulation strategies to identify hard regions in soft tissue organs," *PloS one*, vol. 12, no. 2, p. e0171706, 2017.

[15] K. A. Nichols and A. M. Okamura, "Methods to segment hard inclusions in soft tissue during autonomous robotic palpation," *IEEE Transactions on Robotics*, vol. 31, no. 2, pp. 344–354, 2015.

[16] N. Tanaka, M. Higashimori, M. Kaneko, and I. Kao, "Noncontact active sensing for viscoelastic parameters of tissue with coupling effect," *IEEE Transactions on Biomedical Engineering*, vol. 58, no. 3, pp. 509–520, 2011.

[17] T. Kawahara, S. Tanaka, and M. Kaneko, "Non-contact stiffness imager," *The International Journal of Robotics Research*, vol. 25, no. 5-6, pp. 537–549, 2006.

[18] J. Bergström and M. Boyce, "Constitutive modeling of the large strain time-dependent behavior of elastomers," *Journal of the Mechanics and Physics of Solids*, vol. 46, no. 5, pp. 931–954, 1998.

[19] E. M. Arruda and M. C. Boyce, "A three-dimensional constitutive model for the large stretch behavior of rubber elastic materials," *Journal of the Mechanics and Physics of Solids*, vol. 41, no. 2, pp. 389–412, 1993.

[20] A. E. Kerdok, P. Jordan, Y. Liu, P. S. Wellman, S. Socrate, and R. D. Howe, "Identification of nonlinear constitutive law parameters of breast tissue," in *Proceeding of 2005 summer Bioengineering Conference, June*, 2005, pp. 22–26.

[21] Y. Liu, A. E. Kerdok, and R. D. Howe, "A nonlinear finite element model of soft tissue indentation," in *Medical Simulation*. Springer, 2004, pp. 67–76.

[22] K. Sangpradit, H. Liu, P. Dasgupta, K. Althoefer, and L. D. Seneviratne, "Finite-element modeling of soft tissue rolling indentation," *IEEE Transactions on Biomedical Engineering*, vol. 58, no. 12, pp. 3319–3327, 2011.

[23] G. Chagnon, M. Rebouah, and D. Favier, "Hyperelastic energy densities for soft biological tissues: a review," *Journal of Elasticity*, vol. 120, no. 2, pp. 129–160, 2015.

[24] E. J. Patterson, C. H. Scudamore, D. A. Owen, A. G. Nagy, and A. K. Buczkowski, "Radiofrequency ablation of porcine liver in vivo: effects of blood flow and treatment time on lesion size," *Annals of surgery*, vol. 227, no. 4, p. 559, 1998.

[25] A. Kutikov and R. G. Uzzo, "The renal nephrometry score: a comprehensive standardized system for quantitating renal tumor size, location and depth," *The Journal of urology*, vol. 182, no. 3, pp. 844–853, 2009.